Revista Brasileira de Cartografia
ISSN 1808-0936 | https://doi.org/10.14393/revbrascartogr
Sociedade Brasileira de Cartografia, Geodésia, Fotogrametria e Sensoriamento Remoto

Study on Vertical Crustal Deformations in Ecuador Based on GPS Data and Surface Loading Models

Estudo das Deformações Verticais Terrestres Ocorrentes no Equador Baseado em Dados GPS e Modelos de Carga Superficiais

Christian Pilapanta [1] e Claudia Krueger [2]

1 Universidade Federal do Paraná. Curso de Pós-graduação em Ciências Geodésicas, Curitiba, Brasil. christian.pilapanta@ufpr.br.
ORCID: https://orcid.org/0000-0003-1155-7173
2 Universidade Federal do Paraná. Curso de Pós-graduação em Ciências Geodésicas, Curitiba, Brasil. ckrueger@ufpr.br.
ORCID: https://orcid.org/0000-0002-4839-1317

Received: 01.2023 | Accepted: 05.2023

Abstract: The largest mass redistribution on the solid Earth's surface occurs as part of the hydrological cycle. These processes load and deform the solid Earth and consequently, an elastic response of the crust is induced. The general approach to predict this response involves the convolution of Green's functions and mass distribution models. Nevertheless, these models together do not conserve their global mass and the estimation of a total response by combining individual phenomena is not self-consistent. To solve this, a passive ocean response commonly is included. In order to study this process and its effects in the positions of geodetic sites, we compare 47 GPS vertical time series belonging to the continuous monitoring GNSS network of Ecuador and their respective loading signals over the last 20 years (2000 – 2020). The results indicate a moderate correlation between all the GPS heights and their loading signals and a reduction in the weighted root mean square (WRMS) in 35 of the 47 stations after filtering the total response, its value being higher in those stations with heights less than 3000 meters.
Keywords: GPS. Passive ocean response. Seasonal mass changes.

Resumo: Em uma série temporal com extensa base de dados, a maior redistribuição de massas na superfície da Terra sólida ocorre em função do ciclo hidrológico. Este processo, carrega e deforma a Terra e consequentemente, induz à uma resposta elástica da sua superfície. Geralmente, a modelagem empregada envolve a convolução das chamadas Funções de Green e diferentes modelos de distribuição de massas. No entanto, estes modelos não conservam suas massas globais através do tempo e a estimativa de uma resposta total através da sua combinação individual e não podem ser considerados auto consistente. Visando solucionar este problema, frequentemente, é incluída uma resposta oceânica "passiva" capaz de manter a superfície do oceano numa superfície equipotencial média mesmo quando mudar sua massa. Objetivando o estudo destes processos e seus efeitos na componente vertical de várias estações geodésicas, foram comparadas as series de coordenadas de 47 estações GPS da Rede GNSS de monitoramento contínuo do Equador e seus respectivos sinais de carga durante os últimos 20 anos (2000 – 2020). Mediante uma análise dos resultados foi verificada uma correlação moderada entre as altitudes e os sinais de carga. Além disso, ocorreu uma redução no erro quadrático médio ponderado (WRMS) para 35 das 47 estações consideradas neste estudo após filtrada a resposta elástica total. A maior redução ocorreu nas estações com altitudes de até 3000 metros.
Palavras-chave: GPS. Resposta oceânica passiva. Movimentos de massa.

1 INTRODUCTION

It is well known that the largest mass redistribution on the solid Earth's surface mainly occurs as part of the hydrological cycle (VAN DAM; WAHR, 1998). These processes load and deform the solid Earth and consequently, an elastic response of the Earth's crust is induced.

Depending on geographic location, this response can be range from millimetres to several centimetres in amplitude (MARTENS, 2016), leading to the displacement of the geodetic sites both vertically and horizontally on annual to sub-diurnal time scales and being necessary for its pre-analysis in the use of space geodetic observations (WIJAYA et al., 2013).

Changes in the Earth's gravitational field, its angular momentum, and the moments of inertia of the atmosphere, ocean, and terrestrial hydrosphere are also some of the main terrestrial parameters affected by this mass redistribution (PLAG; BLEWITT; HERRING, 2007). To correct these variations, different models of surface mass loads are used (i.e., atmospheric, oceanic and hydrological models). The displacement-response is then calculated by convolving the individual models with the loading Green's function (LGFs) (LONGMAN, 1962, 1963), which describes the unit response of the Earth as a function of load and response location (CLARKE, 2005).

For that, typically a self-gravitating, spherically symmetric, non-rotating, elastic and isotropic (SNREI) Earth model, such as PREM (DZIEWONSKI; ANDERSON, 1981) or ak135 model (KENNETT; ENGDAHL; BULAND, 1995) is assumed. In this case, the Green's function only depends on load-response separation and does not take into account the lateral heterogenicity in Earth structure or the mantle anelasticity (MARTENS; RIVERA; SIMONS, 2019).

However, obtaining the surface mass load estimates separately, leads to a particular problem, because, as was demonstrated by Clarke (2005), these models together do generally not conserve their global mass and a total response, simply combining individual phenomena is not self-consistent. To solve this, an additional term that considers the mass exchange in a gravitationally consistent integrated model of the Earth system is required (BLEWITT; CLARKE, 2003).

The so-called sea-level loading signal fulfils this purpose. It is derived by solving the sea-level equation (FARRELL; CLARK, 1976) for the total mass of terrestrial water storage and atmospheric surface pressure (DILL; DOBSLAW, 2013), adding a uniform layer of water to the ocean model and allowing the ocean to respond tidally to the total load's gravitational potential and, therefore, forcing the total load mass to be conserved (CLARKE, 2005).

Based on this, this study investigates the incidence of the individual and total loading signals (i.e., non-tidal atmospheric loading, non-tidal oceanic loading, hydrological loading and sea-level equation loading) in the long-term stability and repeatability of 47 GPS vertical time series located in continental Ecuador. The LGFs have been derived using load Love numbers (LLNs) in the centre of figure (CF) frame (PLAG; BLEWITT; HERRING, 2007) considering the ak135 model (KENNETT; ENGDAHL; BULAND, 1995) as the standard elastic Earth model. The use of the ak135 model is because it is the standard model used and recommended by IASPEI (International Association of Seismology and Physics of the Earth's Interior) in the analysis of movements of the Earth's crust and surface.

2 EARTH DEFORMATION INDUCED BY SURFACE MASS LOADING

2.1 Load Love numbers computation

As mentioned by Martens (2016), the Love numbers (LNs) are dimensionless parameters that characterize the yielding of the elastic Earth to body forces and surface tractions. The first three LNs (i.e., h_n, k_n and l_n) were introduced by Love (1909) and Shida (1912), respectively, to characterize the Earth's response to the potential or force without loading the Earth's surface (VAN DAM, 2017). For describing the response to the surface load, a second class of LNs (i.e., h'_n, k'_n and l'_n), referred to as load Love numbers (LLNs) were adopted. The elastic LLNs are computed by integrating the equation of motion and the Poisson equation inside the Earth, given by Farrell (1972):

$$\nabla \cdot \boldsymbol{\tau} - \nabla(\rho g \boldsymbol{s} \cdot \boldsymbol{e_r}) - \rho \nabla \phi + g \nabla \cdot (\rho \boldsymbol{s}) \boldsymbol{e_r} = 0 \quad (1)$$

$$\nabla^2 \phi = -4\pi G \nabla \cdot (\rho \boldsymbol{s}) \quad (2)$$

where $\boldsymbol{\tau}$ is the incremental stress tensor, ρ and g are the unperturbed density and gravitational acceleration, $\boldsymbol{s}$ is the displacement vector, ϕ is the perturbed gravitational potential, G is the universal gravitational constant and $\boldsymbol{e_r}$ denotes the unit vector of the vertical component.

Therefore, supposing a self-gravitating, spherically symmetric, non-rotating, elastic and isotropic

(SNREI) Earth model (e.g. ak135 model) with certain boundary conditions at the surface, the solution of Eq. (1) and Eq. (2) can be transformed and expressed by the Eq. (3) and Eq. (4):

$$\mathbf{s} = \sum_{n=0}^{\infty} \left(U_n(r) P_n(\cos\psi) \boldsymbol{e_r} + V_n(r) \frac{\partial P_n(\cos\psi)}{\partial \psi} \boldsymbol{e_v} \right) \tag{3}$$

$$\phi = \sum_{n=0}^{\infty} \Phi_n(r) P_n(\cos\psi) \tag{4}$$

where U_n, V_n and Φ_n are radial coefficients of the spherical harmonic expansions (i.e., transformed variables indicating vertical displacements, tangential displacements and potential, respectively), $\boldsymbol{e_v}$ denotes the vector of the horizontal component and $P_n(\cos\psi)$ is a Legendre polynomial of order n.

With further simplifications applied, the elastic LLNs can be further related to the transformed variables, according to:

$$\begin{bmatrix} U_n(r) \\ V_n(r) \\ \Phi_n(r) \end{bmatrix} = \mathrm{W}(r) \begin{bmatrix} \frac{h'_n(r)}{g} \\ \frac{l'_n(r)}{g} \\ k'_n(r) \end{bmatrix} \tag{5}$$

where $\mathrm{W}(r)$ represents the potential induced by the point mass. Solving and integrating Eq. (5) from the inner Earth to the surface, gives the set of LLNs which are based on the given SNREI Earth model (VAN DAM, 2017).

2.2 Green's function approach

As mentioned by van Dam (2012), using the LLNs for calculating the surface displacements due to a surface mass load is fine when the load is global. However, if we are interested in geographically restricted loads, the Green's function approach is more convenient to be used. Thus, substituting Eq. (5) in Eq. (3) and Eq. (4), we obtain the so-called elastic loading Green's functions (LGFs) for the radial (u_r) and tangential (u_t) displacements, evaluated at the Earth's surface and expressed by Eq. (6) and Eq. (7):

$$\mathrm{G}_{u_r} = \frac{R}{M} \sum_{n=0}^{\infty} h'_n P_n(\cos\psi) \tag{6}$$

and

$$\mathrm{G}_{u_t} = \frac{R}{M} \sum_{n=0}^{\infty} l'_n \frac{\partial P_n(\cos\psi)}{\partial \psi} \tag{7}$$

where R is the mean Earth radius, M represents the mass of the Earth and ψ is the angular distance between the load and the observation point.

The LLNs become constant at large n (i.e., $h'_\infty, k'_\infty, l'_\infty$). In that case, the LGFs can also be expressed analytically using a Kummer's transformation (KUMMER, 1837), such as:

$$G_{u_r} = \frac{R}{2M}\frac{h'_\infty}{\sin(\psi/2)} + \frac{R}{M}\sum_{n=0}^{\infty}(h'_n - h'_\infty)P_n(\cos\psi) \tag{8}$$

$$G_{u_t} = -\frac{R}{M}l'_\infty\frac{\cos(\psi/2)[1+2\sin(\psi/2)]}{2\sin(\psi/2)\,[1+\sin(\psi/2)]} + \frac{R}{M}\sum_{n=0}^{\infty}(nl'_n - l'_\infty)\frac{1}{n}\frac{\partial P_n(\cos\psi)}{\partial\psi} \tag{9}$$

In practice, the LLNs computations are often carried out to spheric harmonic degree n = 10000, whereby, only a finite number of terms are required to evaluate the second summation in Eq. (8) and Eq. (9), and the LLNs are assumed to be equivalent to the asymptotic values (MARTENS, 2016).

The surface displacements generated by surface mass loading depend both on the physical characteristics of the deformation as well as the chosen reference frame (BLEWITT, 2003). In this way, the calculation of LLNs and corresponding LGFs is computed in a reference frame fixed to the centre of mass of the solid Earth, abbreviated commonly as CE. The CE frame is convenient for mathematical computation but not directly observable in practice (MARTENS, 2016).

A more appropriate reference frame for GNSS inferred surface displacements is one fixed to the centre of mass of the entire Earth system, abbreviated as CM. It includes the solid Earth as well as its fluid exterior (i.e., oceans and atmosphere) and it is resembled through the definition of the International Terrestrial Reference Frame (ITRF) origin in the long-term sense. Lastly, and as was mentioned by Ferreira et al. (2019) for seasonal and other short time scales, the origin of the ITRF is indistinguishable from the centre of the figure, abbreviated as CF, and commonly used in the coordinate time series analysis when long-term trends and offsets are removed.

2.3 Spatial convolution over the loading area

Finally, considering a surface mass load $\Delta\sigma$, located at point $\boldsymbol{r}'$, given by the latitude φ' and longitude λ'. The radial deformation Δr evoked by this surface mass load at any point $\boldsymbol{r}$ with latitude φ and longitude λ, involves the convolution of elastic LGFs and the different load models (i.e., non-tidal atmospheric loading (NTAL), non-tidal oceanic loading (NTAL) and hydrological loading (HYDL)):

$$\Delta r(\varphi,\lambda) = R^2\int\int_{\Omega}\Delta\sigma(\varphi',\lambda')G(\psi)d\Omega \tag{10}$$

where R is the mean Earth radius, $d\Omega = \cos\varphi'\,d\varphi' d\lambda'$ is the surface element of the unit sphere and $G(\psi) = G_{u_r}(\psi)$ is the Green's function for the radial displacements per kg load, given by Eq. (6). The integral in Eq. (10) is taken over the surface area of the Earth, Ω.

2.4 Mass conservation on seasonal surface mass loading models

As explained by Clarke (2005), models of surface loading obtained by simply combining the mass redistribution due to individual phenomena will not in general be self-consistent. This is because most oceanic models make use of the Boussinesq approximation (LAMB, 1901), which in principle conserves ocean volume rather than ocean mass. To solve this, it is necessary to introduce the barystatic variations to obtain the conservation of the global mass.

So, considering an SNREI Earth model and expressing the loading signals in terms of the equivalent height of a column of seawater with density ρ_s, the total time-variable load T can be calculated as a function of geographic position Ω as:

$$T(\Omega) = D(\Omega) + S(\Omega) = \sum_{n=1}^{\infty}\sum_{m=0}^{n}\sum_{\Phi=C}^{S} T_{nm}^{\Phi} Y_{nm}^{\Phi}(\Omega) \tag{11}$$

where, T_{nm}^{Φ} and $Y_{nm}^{\Phi}(\Omega)$ are un-normalized surface spherical harmonic basis functions calculated according to established by Blewitt; Clarke (2003); $D(\Omega)$ represents the dynamic load and $S(\Omega)$ is the so-called passive oceanic load defined as the change in ocean bottom pressure and expressed as:

$$S(\Omega) = C(\Omega)\left[\frac{\Delta V}{g} + \sum_{n=1}^{\infty}\sum_{m=0}^{n}\sum_{\Phi=C}^{S}\left(\frac{3\rho_s}{\rho_e}\frac{1+k'_n-h'_n}{2n+1}\right)T_{nm}^{\Phi} Y_{nm}^{\Phi}(\Omega)\right] \tag{12}$$

the $C(\Omega)$ term is the ocean function, defined as zero over land and unity over the oceans and $\Delta V/g$ represents the deformation of the geoid because of the irregular distribution of oceans and land and ocean-continent mass exchange. ρ_e is the mean density of the solid Earth.

3 DATA AND METHODS

3.1 GPS coordinate time series

In this study, we have used 2 types of positional solutions obtained for 47 GPS sites located in Continental Ecuador over the last 20 years (Figure 1).

Figure 1 – GPS sites location.

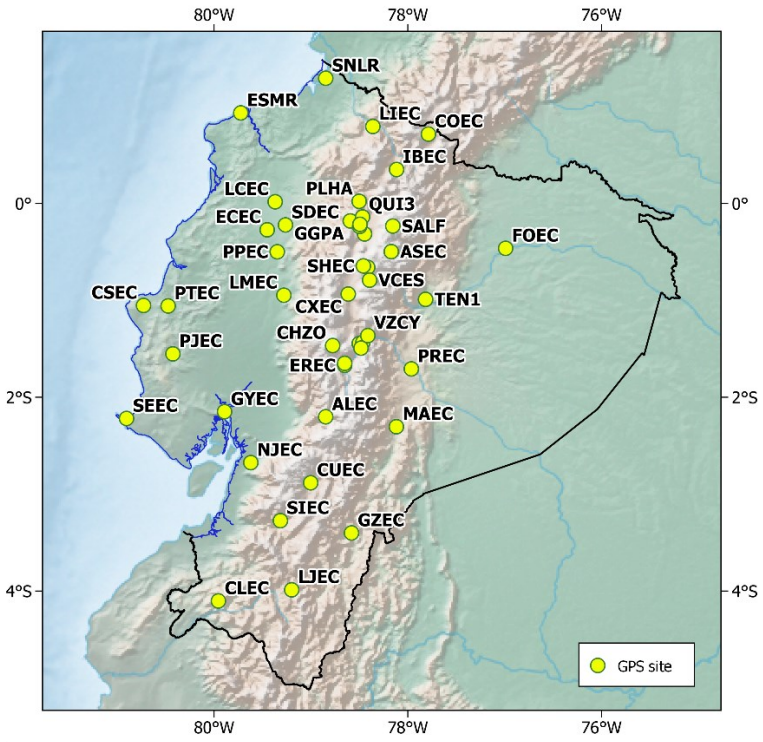

Source: The authors (2023).

First, daily precise point positioning (PPP) solutions provided by the Nevada Geodetic Laboratory (NGL) and processed according to NGL/UNR GPS Data Analysis Strategy (BLEWITT; HAMMOND; KREEMER, 2018) and second, weekly solutions provided by the SIRGAS Processing Centres and processed according to the International Earth Rotation Systems Service Conventions (i.e., IERS Conventions 2010)

(PETIT; LUZUM, 2010).

In both solutions, the motions of sites due to oceanic and atmospheric tidal loading were calculated using the coefficients provided by the ocean tide loading for the FES2004 tidal model (LYARD et al., 2006) and the global pressure tidal model developed by Ponte e Ray (2002), respectively.

In the case of NGL solutions, these are aligned to the IGS14 reference frame of the International GNSS Service (IGS), compatible with the latest release of the International Terrestrial Reference Frame (i.e., ITRF2014) (ALTAMIMI et al., 2016) through the use of orbital and clock products obtained from the second IGS reprocessing campaign (INTERNATIONAL GNSS SERVICE, 2013).

On the other hand, the SIRGAS solutions computed before GPS week 1400 are reprocessed using the first IGS reprocessing campaign products (INTERNATIONAL GNSS SERVICE, 2005) to include absolute corrections for the phase centre variations of the GNSS antenna (SÁNCHEZ; DREWES, 2016), which in turn are referred to the IGS05 reference frame. For that reason, the SIRGAS solutions are aligned to different IGS reference frames, depending on the date to which it is referred (i.e., IGS05, IGS08, IGb08 and IGS14).

The effect of the datum change on the heights of SIRGAS solutions will be considered to be a "jump" within the trajectory model (BEVIS; BROWN, 2014) in a similar way as established by Montecino et al. (2017).

3.2 Loading models

Three main mass distribution models have been used for this study. These are the non-tidal atmospheric loading (NTAL), non-tidal oceanic loading (NTOL) and hydrological loading model (HYDL).

Atmospheric mass loads are derived from 3-hourly non-tidal atmospheric surface pressure data given by ERA-40 (KALLBERG et al., 2007) and ERA-INTERIM (BERRISFORD et al., 2011) models of the European Centre for Medium-Range Weather Forecasts (ECMWF). Oceanic mass loads are derived from 3-hourly non-tidal ocean bottom pressure data given by the ocean model MPIOM (DOBSLAW et al., 2017). Finally, hydrological mass loads are given from the global hydrological model LSDM with a temporal resolution of 24h (DILL, 2008).

As mentioned in the section 2.4. because the 3 models together (i.e., NTAL, NTOL and HYDL) do generally not conserve their global mass, a barystatic sea-level variations model is necessary (i.e., sea-level variations are not included in the oceanic contribution NTOL). For that, sea-level mass loads are derived by solving the sea-level equation for the total mass of terrestrial water storage and atmospheric surface pressure according to the procedure established by Clarke (2005).

All models have been resampled on a regular 0.5° x 0.5° global grid and daily intervals to be compatible with the PPP solutions used.

3.3 Consistency analysis of Loading signals

To evaluate the consistency of the different loading signals concerning the GPS solutions, we used two principal parameters: the Pearson's correlation, calculated from the linear fitting of the correlation plot and the weighted root mean square error reduction ($WRMS_{RED}$) expressed by Eq. (13) as:

$$WRMS_{RED} = \frac{WRMS_{GPS} - WRMS_{GPS-LOAD}}{WRMS_{GPS}} \times 100\% \quad (13)$$

where, $WRMS_{GPS}$ is the weighted RMS of the GPS coordinate time series and $WRMS_{GPS-LOAD}$ is the weighted RMS of the GPS series corrected from one of the loading models.

As mentioned by Ferreira et al. (2019), larger positive $WRMS_{RED}$ values indicate better agreement between loading signals and GPS coordinates. Conversely, larger negative $WRMS_{RED}$ values indicate worse agreement.

 DOI: http://dx.doi.org/10.14393/rbcv75n0a-67887

4 RESULTS AND DISCUSSION

4.1 Loading signals analysis

Figure 2 shows the detrended vertical coordinate time series for 4 of the 47 GPS sites together with the individual loading signals calculated for each one.

Figure 2 – Loading signals and coordinate time series of GPS sites: BIEC, RIOP, S061 and SHEC.

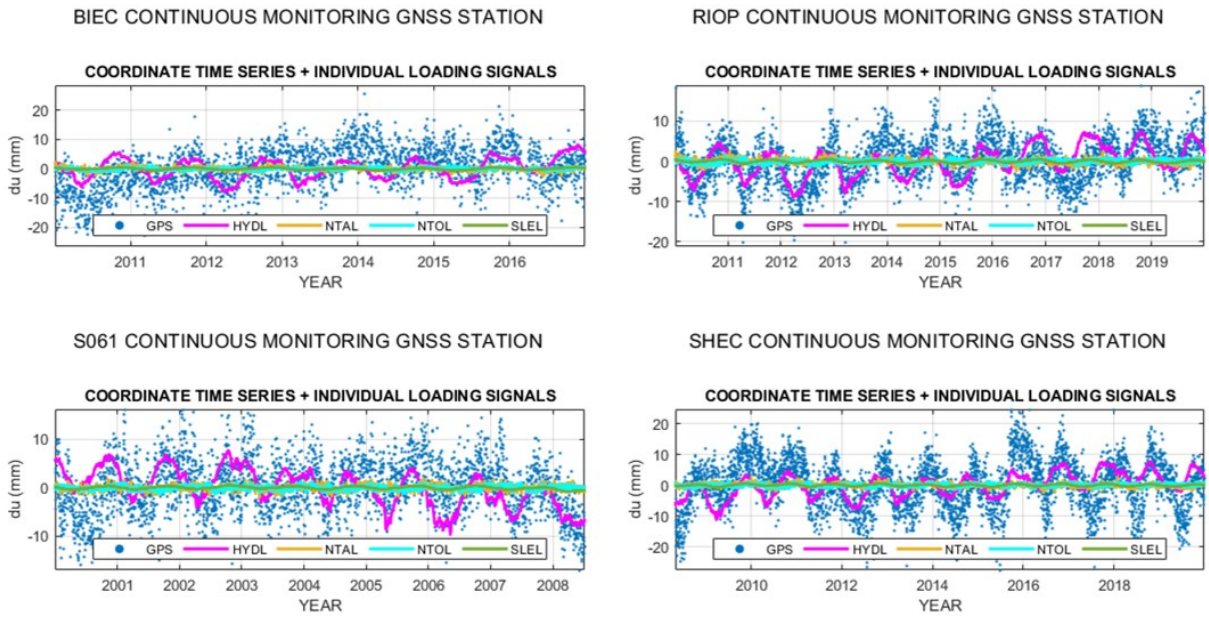

Source: The authors (2023).

Note how all the signals follow the trend of the time series, with the hydrological loading signal (HYDL) being the one with the greatest amplitude, followed by the non-tidal atmospheric loading signal (NTAL), non-tidal oceanic loading signal (NTOL) and sea-level equation loading signal (SLEL), respectively.

This can be clearly seen in Figure 3, which shows the amplitudes for each signal as a function of the ellipsoidal height of the GPS sites.

Figure 3 – Amplitude of individual loading signals as a function of the height of GPS sites.

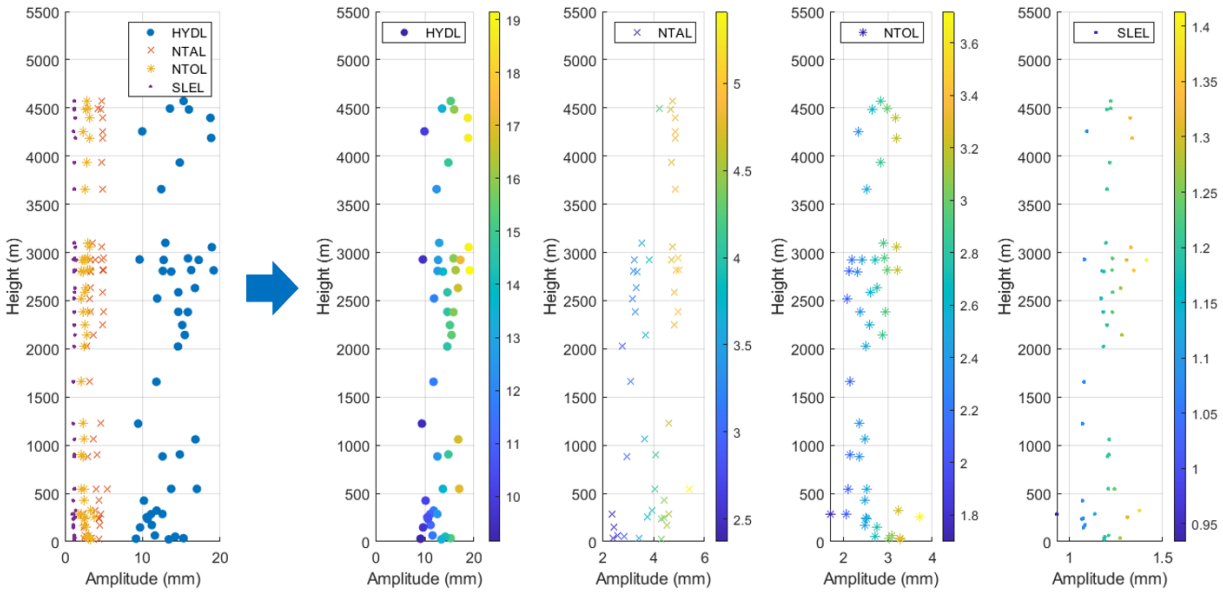

Source: The authors (2023).

In this, it is possible to see how, in the case of the HYDL signal, its amplitudes can reach values close to 20 mm, different from what happens with the NTAL and NTOL signals, whose values reach a maximum of 6 mm and 4 mm, respectively. Finally, for the case of the SLEL signal, its highest values are around 1 mm. For all signals, their highest amplitudes are concentrated at sites above 2000 meters high, that is, sites located in the Andean region of Ecuador.

Figure 4 and Figure 5 show the total loading signals and their amplitudes as a function of sites location, one of them being calculated as the sum of the HYDL, NTAL and NTOL signals and called the HAO loading signal and, the other, obtained through the incorporation of the SLEL signal (i.e., HYDL + NTAL + NTOL + SLEL) and called the HAOS full loading signal.

Figure 4 – Total loading signals and time series of GPS sites: BIEC, RIOP, S061 and SHEC.

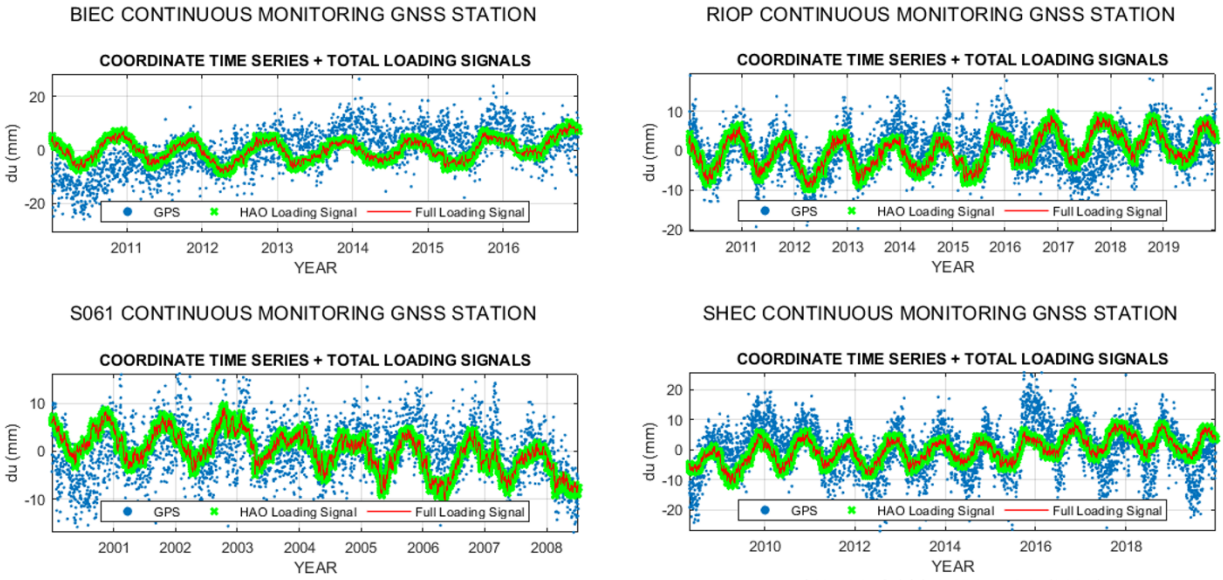

Source: The authors (2023).

Figure 5 – Amplitude of total loading signals as a function of GPS sites locations.

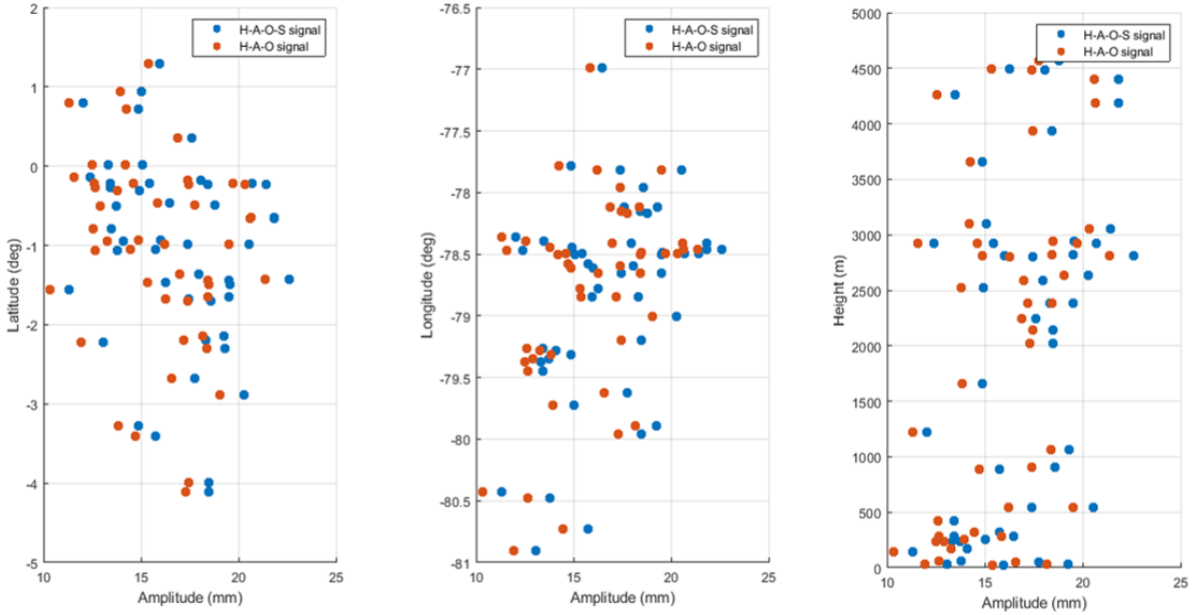

Source: The authors (2023).

Due to the small amplitudes of the SLEL loading values, the HAO and HAOS loading signals can be considered similar, however, there are significant differences in their amplitudes which are around 0.5 mm and

1.5 mm (see Figure 5). In a similar way as for the individual signals, for the 2 total signals, their highest amplitude values are concentrated in sites with heights greater than 2000 meters high, however, there is no predefined pattern concerning their geographical location (i.e., latitude and longitude).

4.2 Comparison of loading signals and GPS solutions

To evaluate the consistency of the different loading signals concerning the GPS solutions, Pearson's correlation and WRMS reduction factors ($WRMS_{RED}$) were calculated.

Figure 6 shows the individual WRMS reduction factor histograms for each of the loading signals and Figure 7 shows these parameters for each of the 2 total loading signals as a function of the GPS site's heights.

Figure 6 – WRMS reduction factor (%) histograms for each loading signals.

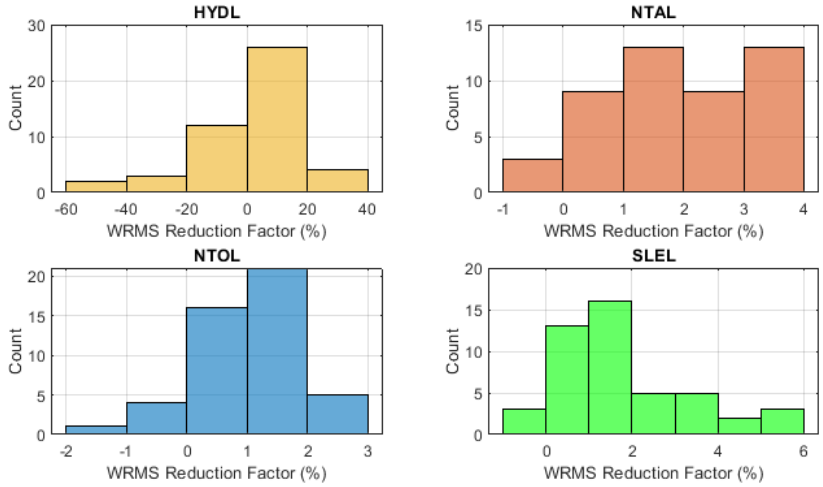

Source: The authors (2023).

Figure 7 – Pearson's correlation and WRMS reduction factor (%) for total loading signals.

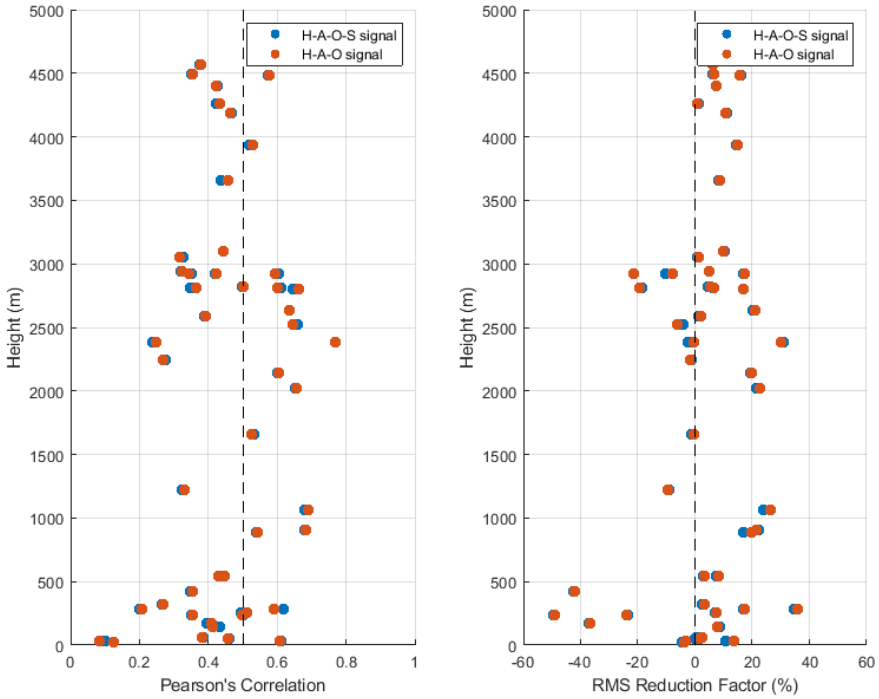

Source: The authors (2023).

In general, it is possible to see a moderate correlation between all the GPS heights and their total loading signals and consequently a reduction in their WRMS values. Thus, 32 GPS sites obtained an

improvement in their WRMS after filtering the HAO loading signal and 33 GPS sites after filtering the HAOS loading signal. It is also important to note, how some sites, obtained a degradation of their accuracy after filtering the loading signal (i.e., negative $WRMS_{RED}$ values). Despite the HAO loading signal being the one that achieved the greater $WRMS_{RED}$ values, it is important to note how through the individual analysis of the loading signals, the SLEL has a greater impact on the WRMS reduction of the sites when compared to the others, improving the accuracy of heights in 44 of the 47 GPS sites analysed. This is followed by the NTAL, NTOL and HYDL signal with a WRMS reduction in 44, 42 and 30 GPS sites, respectively.

Finally, Figures 8 and 9 show the original and modified coordinate time series for the RIOP GPS site after the HAO loading signal is filtered and the spatial distribution of these 2 parameters obtained for each of the 2 total loading signals.

Figure 8 – Original and filtered GPS coordinate time series for RIOP GPS site.

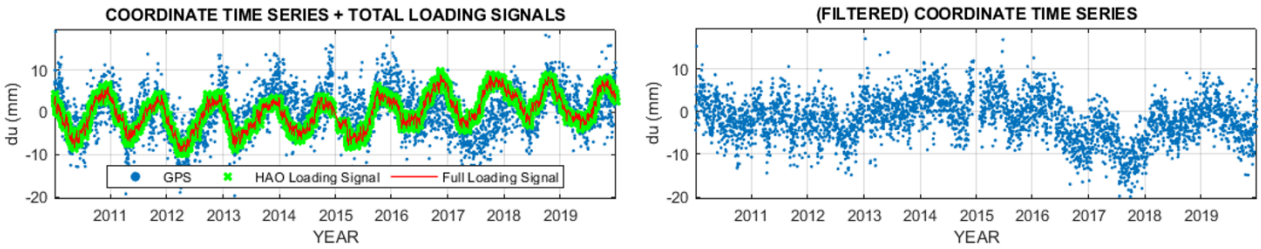

Source: The authors (2023).

Figure 9 – Pearson's correlation and WRMS reduction factor (%) for total loading signals.

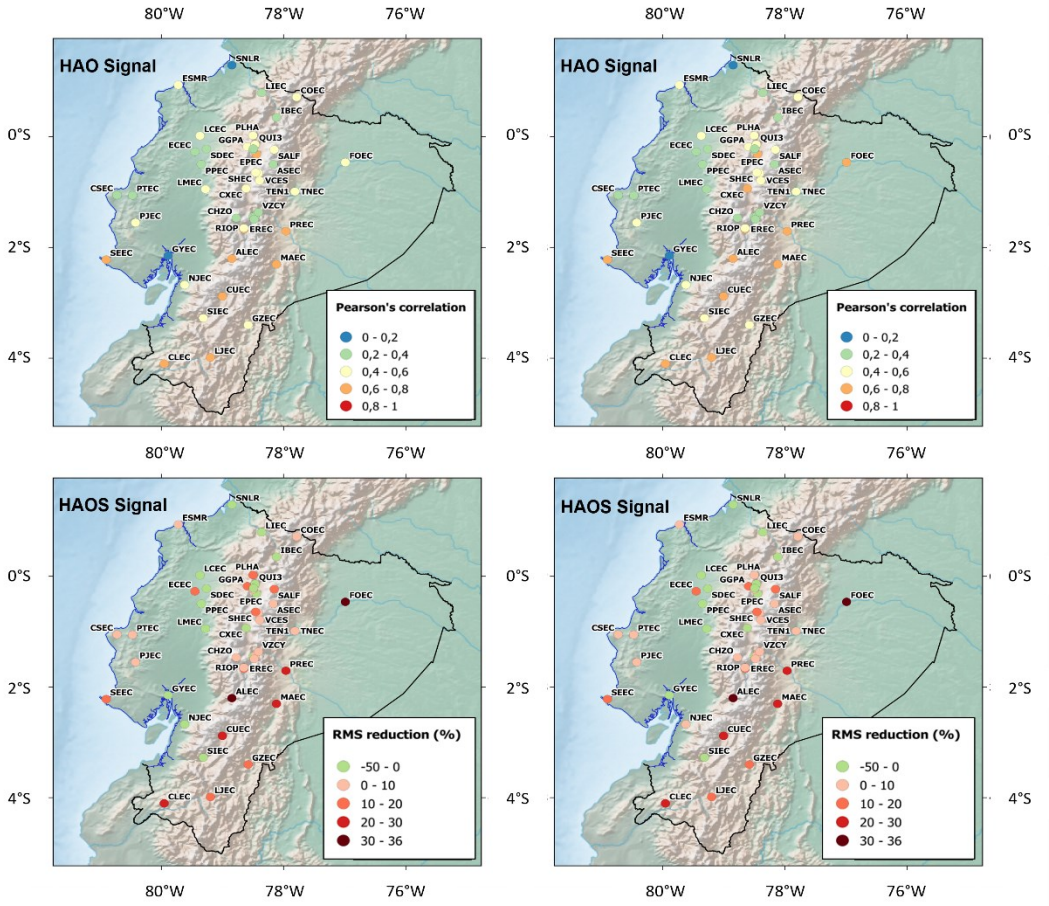

Source: The authors (2023).

Although there is no particular spatial pattern, it is possible to see how most of the sites that obtained an improvement in their WRMS and with a Pearson's correlation greater than +/-0.4 (moderate correlation)

are located in the Andean region and Amazon basin regardless of the total loading signal analysed.

All the final coordinate time series for each of the GPS sites analysed, as well as the entire data set (i.e., surface loading signals, GPS solutions, earth data model, LLNs and LGFs), can be obtained at Pilapanta e Krueger (2022) (open dataset repository).

5 CONCLUSIONS

In this study, we evaluate the consistency of the different loading signals concerning the GPS coordinates through the analysis of the positioning solutions for 47 GPS sites located in Continental Ecuador.

In general, it was possible to show the existence of a moderate correlation between the GPS heights and their loading signals for most of the sites analysed, being that for all signals (i.e., HYDL, NTAL, NTOL and SLEL), their highest amplitudes are concentrated at sites above 2000 meters high, that is, sites located in the Andean region of continental Ecuador.

It was also possible to see a reduction in the WRMS of 33 stations after filtering the HAO loading signal and in 32 stations after filtering the HAOS full loading signal. Although there is no substantial difference in the total load signal with the incorporation of the SLEL, it is important to note that, through the individual analysis of the loading signals, it has a greater impact on the WRMS reduction of the sites when compared to the others, improving the accuracy of heights in 44 of the 47 GPS sites analysed. It is followed by the NTAL, NTOL and HYDL signal with an improvement of the WRMS in 44, 42 and 30 GPS sites, respectively.

Finally, through the spatial analysis of the data, it was possible to see how most of the sites that obtained an improvement in their WRMS are located in the Andean region and Amazon basin, regardless of the total loading signal analysed.

Acknowledgements

The authors would like to thank the Coordination for the Improvement of Higher Education Personnel (CAPES) for their financial support and SIRGAS and NGL for making publicly available the position time series used in this study.

Author's Contribution

The two authors were responsible for the research, conceptualization, writing, revision and final edition.

Conflicts of Interest

The authors inform that there are no conflicts of interest.

References

ALTAMIMI, Z.; REBISCHUNG, P.; MÉTIVIER, L.; COLLILIEUX, X. ITRF2014: A new release of the International Terrestrial Reference Frame modeling nonlinear station motions. **Journal of Geophysical Research: Solid Earth**, v. 121, n. 8, p. 6109–6131, 2016. Retrieved from: <http://doi.wiley.com/10.1029/2001JB000561%5Cnhttp://en.scientificcommons.org/43156606%5Cnhttp://www.iers.org/TN36/%5Cnhttps://geo.tuwien.ac.at/fileadmin/editors/GM/GM91_krasna.pdf>. Accessed: 11 jan. 2023.

BERRISFORD, P.; DEE, D.; POLI, P.; BRUGGE, R.; FIELDING, K.; FUENTES, M.; ALLBERG, P.; KOBAYASHI, S.; UPPALA, S.; SIMMONS, A. **The ERA-Interim archive**. 2011.

BEVIS, M.; BROWN, A. Trajectory models and reference frames for crustal motion geodesy. **Journal of**

Geodesy, v. 88, n. 3, p. 283–311, 2014.

BLEWITT, G. Self-consistency in reference frames, geocenter definition, and surface loading of the solid Earth. **Journal of Geophysical Research: Solid Earth**, v. 108, n. B2, 2003.

BLEWITT, G.; CLARKE, P. Inversion of Earth's changing shape to weigh sea level in static equilibrium with surface mass redistribution. **Journal of Geophysical Research: Solid Earth**, v. 108, n. B6, 2003.

BLEWITT, G.; HAMMOND, W.; KREEMER, C. Harnessing the GPS Data Explosion for Interdisciplinary Science. **Eos**, v. 99, 2018. Retrieved from: <https://eos.org/project-updates/harnessing-the-gps-data-explosion-for-interdisciplinary-science>. Accessed: 04 jan. 2023.

CLARKE, P. J. Effect of gravitational consistency and mass conservation on seasonal surface mass loading models. **Geophysical Research Letters**, v. 32, n. 8, p. L08306, 2005. Retrieved from: <http://doi.wiley.com/10.1029/2005GL022441>. Accessed: 03 jan. 2023.

DILL, R. Hydrological model LSDM for operational Earth rotation and gravity field variations. **Scientific Technical Report**, p. 35, 2008. Retrieved from: http://www.google.de/url?sa=t&rct=j&q=hydrological model lsdm for operational earth rotation and gravity field variations&source=web&cd=1&ved=0CEcQFjAA&url=https://e-docs.geo-leo.de/bitstream/handle/11858/00-1735-0000-0001-3286-C/0809.pdf?sequence=1&ei=Sb. Accessed: 04 jan. 2023.

DILL, R.; DOBSLAW, H. Numerical simulations of global-scale high-resolution hydrological crustal deformations. **Journal of Geophysical Research: Solid Earth**, v. 118, n. 9, p. 5008–5017, 2013.

DOBSLAW, H.; BERGMANN-WOLF, I.; DILL, R.; POROPAT, L.; THOMAS, M.; DAHLE, C.; ESSELBORN, S.; KÖNIG, R.; FLECHTNER, F. A new high-resolution model of non-tidal atmosphere and ocean mass variability for de-aliasing of satellite gravity observations: AOD1B RL06. **Geophysical Journal International**, v. 211, n. 1, p. 263–269, 2017.

DZIEWONSKI, A. M.; ANDERSON, D. L. Preliminary reference Earth model. **Physics of the Earth and Planetary Interiors**, v. 25, n. 4, p. 297–356, 1981.

FARRELL, W. E. Deformation of the Earth by surface loads. **Reviews of Geophysics**, v. 10, n. 3, p. 761, 1972. Retrieved from: <http://doi.wiley.com/10.1029/RG010i003p00761>. Accessed: 11 jan. 2023.

FARRELL, W. E.; CLARK, J. A. On Postglacial Sea Level. **Geophysical Journal of the Royal Astronomical Society**, v. 46, n. 3, p. 647–667, 1976.

FERREIRA, V.; NDEHEDEHE, C.; MONTECINO, H.; YONG, B.; YUAN, P.; ABDALLA, A.; MOHAMMED, A. Prospects for Imaging Terrestrial Water Storage in South America Using Daily GPS Observations. **Remote Sensing**, v. 11, n. 6, p. 679, 2019.

INTERNATIONAL GNSS SERVICE. 1st Data Reprocessing Campaign. Retrieved from: <http://acc.igs.org/reprocess.html>. Accessed: 21 apr. 2022.

INTERNATIONAL GNSS SERVICE. 2nd Data Reprocessing Campaign. Retrieved from: <http://acc.igs.org/reprocess2.html>. Accessed: 21 apr. 2022.

KALLBERG, P.; SIMMONS, A.; UPPALA, S.; FUENTES, M. **The ERA-40 Archive**. 2007.

KENNETT, B. L. N.; ENGDAHL, E. R.; BULAND, R. Constraints on seismic velocities in the Earth from traveltimes. **Geophysical Journal International**, v. 122, n. 1, p. 108–124, 1995.

KUMMER, E. Eine neue Methode, die numerischen Summen langsam convergirender Reihen zu berechnen. **Journal für die reine und angewandte Mathematik (Crelles Journal)**, v. 1837, n. 16, p. 206–214, 1837. Retrieved from: <https://www.degruyter.com/document/doi/10.1515/crll.1837.16.206/html>. Accessed: 13 oct. 2022.

LAMB, H. On Boussinesq's Problem. **Proceedings of the London Mathematical Society**, v. s1-34, n. 1, p. 276–284, 1901. Retrieved from: http://doi.wiley.com/10.1112/plms/s1-34.1.276. Accessed: 13 oct. 2022.

LONGMAN, I. M. A Green's function for determining the deformation of the Earth under surface mass loads: 1. Theory. **Journal of Geophysical Research**, v. 67, n. 2, p. 845–850, 1962. Retrieved from:

<http://doi.wiley.com/10.1029/JZ067i002p00845>. Accessed: 12 oct. 2022.

LONGMAN, I. M. A Green's function for determining the deformation of the Earth under surface mass loads: 2. Computations and numerical results. **Journal of Geophysical Research**, v. 68, n. 2, p. 485–496, 1963. Retrieved from: <http://doi.wiley.com/10.1029/JZ068i002p00485>. Accessed: 12 oct. 2022.

LOVE, A. E. H. The yielding of the earth to disturbing forces. **Proceedings of the Royal Society of London. Series A, Containing Papers of a Mathematical and Physical Character**, v. 82, n. 551, p. 73–88, 1909. Retrieved from: <https://royalsocietypublishing.org/doi/10.1098/rspa.1909.0008>. Accessed: 12 oct. 2022.

LYARD, F.; LEFEVRE, F.; LETELLIER, T.; FRANCIS, O. Modelling the global ocean tides: Modern insights from FES2004. **Ocean Dynamics**, v. 56, n. 5–6, p. 394–415, 2006.

MARTENS, H. R. **Using Earth Deformation caused by Surface Mass Loading to Constrain the Elastic Structure of the Crust and Mantle**, 2016. California Institute of Technology.

MARTENS, H. R.; RIVERA, L.; SIMONS, M. LoadDef: A Python-Based Toolkit to Model Elastic Deformation Caused by Surface Mass Loading on Spherically Symmetric Bodies. **Earth and Space Science**, v. 6, n. 2, p. 311–323, 2019.

MONTECINO, H. D.; DE FREITAS, S. R. C.; BÁEZ, J. C.; FERREIRA, V. G. Effects on Chilean Vertical Reference Frame due to the Maule Earthquake co-seismic and post-seismic effects. **Journal of Geodynamics**, v. 112, n. July, p. 22–30, 2017. Elsevier. Retrieved from: <https://doi.org/10.1016/j.jog.2017.07.006>. Accessed: 06 oct. 2022.

PETIT, G.; LUZUM, B. **IERS Conventions (2010)**. Frankfurt am Main, 2010.

PILAPANTA, C.; KRUEGER, C. Dataset. Study of seasonal mass changes and vertical crustal deformations in continental Ecuador based on GPS data and surface loading models. **Mendeley Data**, 2022. Mendeley.

PLAG, H.; BLEWITT, G.; HERRING, T. Towards a Consistent Conventional Treatment of Surface-Load Induced Deformations. **IERS Workshop on Conventions**, 2007. Retrieved from: <www.bipm.org/utils/en/events/iers/Conv_PP2.pdf%0Awww.bipm.info/utils/en/events/iers/Plag_PP2.pdf>. Accessed: 04 oct. 2022.

PONTE, R. M.; RAY, R. D. Atmospheric pressure corrections in geodesy and oceanography: A strategy for handling air tides. **Geophysical Research Letters**, v. 29, n. 24, p. 6-1-6–4, 2002.

SÁNCHEZ, L.; DREWES, H. Crustal deformation and surface kinematics after the 2010 earthquakes in Latin America. **Journal of Geodynamics**, v. 102, p. 1–23, 2016. Elsevier Ltd. Retrieved from: <http://dx.doi.org/10.1016/j.jog.2016.06.005>. Accessed: 10 jan. 2023.

SHIDA, T. On the Body Tides of the Earth, A Proposal for the International Geodetic Association. **Proceedings of the Tokyo Mathematico-Physical Society. 2nd Series**, v. 6, n. 16, p. 242–258, 1912.

VAN DAM, T. M.; WAHR, J. Modeling environment loading effects: A review. **Physics and Chemistry of the Earth**, v. 23, n. 9–10, p. 1077–1087, 1998.

VAN DAM, T. Loading Response of the Earth: Theory and Examples. International Summer School on Space Geodesy and Earth System. **Anais.** 2012. Shanghi. Retrieved from: <http://center.shao.ac.cn/geodesy/school2012/SchoolLecture_Tonie VanTam.pdf>. Accessed: 19 may 2020.

VAN DAM, T. Surface Mass Loading of the Solid Earth: Theory and Examples. EGSIEM Autumn School for Satellite Gravimetry Applications. **Anais**. p.11–15, 2017. Potsdam. Retrieved from: <http://www.egsiem.eu/images/static/Autumn-School/Presentations/van_Dam.pdf>. Accessed: 19 may 2020.

WIJAYA, D. D.; BÖHM, J.; KARBON, M.; KRÀSNÀ, H.; SCHUH, H. Atmospheric pressure loading. **Atmospheric effects in space geodesy**. p.137–157, 2013. Springer.

Author's Biography

Christian G. Pilapanta Amagua was born in Quito, Ecuador in 1989. He holds a degree in Geographical and Environmental Engineering from the Universidad de las Fuerzas Armadas, ESPE, with a MSc and PhD in Geodetic Sciences from the Federal University of Paraná. He has experience in the area of geosciences with an emphasis on Geodesy, Geophysics and Geodynamics. He is currently an Assistant Professor at the Department of Geomatics at the Federal University of Paraná.